www.nature.com/scientificreports

scientific reports

OPEN

Experimental and CFD analysis of flow impediments and encrustation in ureteral stents using in vitro urinary tract model

Md. Didarul Islam[1,2,8], Hyo Jeong Kang[3,8], Sung Jin Tae[3], Kyung-Wuk Kim[4], Young Ho Choi[5], Seung Bae Lee[6], Md Rakibuzzaman[2,7], Min Uk Kim[5]✉ & Hyoung-Ho Kim[3]✉

A significant challenge for urological treatment is caused by encrustation that can obstruct urinary drainage. We analyzed the rate of encrustation formation for the initial three weeks in Conventional Double J Stent (CDJS), Renovated Double J Stent (RDJS), and Single J Stent (SJS) under patient-specific control conditions (37 °C, pH 7.8, 60 mL/hr., 50% stenosis). A conceptually designed in vitro urinary tract model representing the kidney, ureter and bladder model is used where the inlet flow rate is controlled with a peristaltic pump, and when the bladder is filled with artificial urine (AU), it is emptied manually, and the time is measured to calculate flow impediments. Stents have been removed from the tract after 21 days to measure mass and scanning electron microscope (SEM) analysis. A Computational Fluid Dynamics (CFD) analysis has been done to show the velocity profile and wall shear stress (WSS) of stents. RDJS has shown the highest flow rate and stable flow performance from the experiment, and SJS exhibited the lowest encrustation with a mass increase of 0.025 g compared to RDJS (0.053 g) and CDJS (0.057 g). The SEM image showed encrustation covered 10.37% of the SJS significantly lower than RDJS (13.04%) and CDJS (13.52%) near the stenosis side holes. The research evidence on SJS demonstrates the least encrustation of SJS stenosis region is further validated through the simulation result which showed a higher wall shear stress (10.4 mPa) for SJS at that location. SJS should be used for short durations for high-risk patients and RDJS for better flow maintenance, which indicates that stent selection should focus on improving the patient's outcomes.

Ureteral stents are the most used medical device for patients with urological difficulties to carry urine to the bladder from the kidneys during stenosis or obstruction caused by stones, tumors, and post-surgical complications[1,2]. Since the initial introduction of stents in 1978, the use and development process has continued to evolve until today[3]. Therefore, different types of stents are placed in the human urinary tract based on individuals' urology-related difficulties worldwide[4]. Despite being used widely, these stents can cause several problems with encrustation being one of the most significant.

Encrustation involves the deposition of crystals on the interior and exterior surfaces of the ureteral stent[5]. Stent occlusion, urinary tract infections (UTIs), and pain can result from irritation or obstruction due to the gradual buildup of mineral deposits on surgical sites[6,7]. To be precise, this encrustation occurs when urinary salts such as calcium oxalate, struvite (magnesium ammonium phosphate), and uric acid precipitate and form crystalline layers on the surfaces of stents, disrupting urine flow and leading to complications[8,9]. These deposits are influenced by the chemical composition of urine and the surface properties of the stent material, and the progression of encrustation causes patient discomfort conditions that severely diminish quality of life and require urgent medical intervention[10–12].

[1]Department of Mechanical Engineering, Graduate School of Engineering, Gyeongsang National University, Jinju, South Korea. [2]Department of Mechanical Engineering, International University of Business Agriculture and Technology, Dhaka, Bangladesh. [3]School of Aerospace Engineering, Gyeongsang National University, Jinju, South Korea. [4]Clean Disinfection, Seoul, South Korea. [5]Dept. of Radiology, College of Medicine, Seoul National University, SMG-SNU Boramae Medical Center, Seoul, South Korea. [6]Department of Urology, Burjeel Hospital, Abu Dhabi, UAE. [7]Research Centre of Fluid Machinery Engineering and Technology, Jiangsu University, Zhenjiang 212013, China. [8]Md. Didarul Islam and Hyo Jeong Kang are the co-first authors. ✉email: alsl0079@gmail.com; khh106@gnu.ac.kr

In the urinary tract, urine is stored in the bladder of the urinary system and is released several times a day as per the natural process of the human body. This bladder is an elastic organ whose biochemical properties of its wall ensure the capability of slowly distending under low pressure to contain a large volume of urine[13]. The average volume of urine in the bladder ranges from 200 to 700 mL[14]. The ureterovesical junction (UVJ) connects the ureter and bladder through the ureteric orifice which acts as an inlet while the urethra acts as an outlet[15]. Over the years researchers have used In Vitro bladder models made of different materials like glass, fermentation flasks, polythene boxes/vessels, and plastic bags for experimental purposes[16–22].

Furthermore, in vitro urinary tract experimental models are used for analyzing encrustation under controlled laboratory conditions[23]. Agarwal et al.[24] introduced a temperature-controlled, water-jacketed flow system using sterile artificial urine (AU) to simulate physiological conditions, which served as a foundation for our temperature control strategy. Hu et al.[25] developed a low-flow pump system to model urine movement between the kidney and bladder reservoirs, informing our approach to simulating realistic flow rates. Shaokai et al.[26] employed laser sheet visualization and pressure sensors to understand flow dynamics across stents, which underscored the importance of pressure measurement and visualization techniques in our design. Choi et al.[27] introduced a physical stenotic model to assess pressure drops across ureteral stents, directly linking mechanical obstruction with flow performance, an approach we adapted for our current 50% stenosis model. Shilo et al.[28] incorporated piezometric measurements in a synthetic ureter model to assess pressure responses during simulated urine flow, thus emphasizing the role of pressure buildup in stent performance evaluations.

Computational Fluid Dynamics (CFD) has emerged as a valuable tool that enables detailed visualization of urine flow behavior, pressure distributions, and regions of stagnation that may be prone to encrustation. By simulating various stent geometries and flow conditions, CFD assists in identifying design features that minimize stagnant flow zones and improve overall performance[29–31]. Such simulations complement experimental studies by offering mechanistic insights that are otherwise difficult to obtain in a clinical or in vitro setup.

This study uses an In Vitro experiment using a conceptually designed bladder model with artificial urine to evaluate the encrustation formation and flow performance of three different kinds of ureteral stents, along with CFD simulations to validate numerically. These three types of ureteral stents are the Conventional Double J Stent (CDJS), a standard 6 Fr, 226 mm stent with 32 side holes; the Renovated Double J Stent (RDJS), a modified version of the CDJS featuring 44 side holes to enhance flow dispersion; and the Single J Stent (SJS), which is 113 mm in length with 18 side holes and derived by cutting a CDJS in half. Integrating in vitro data such as stent mass and flow rate from the experimental findings with the scanning electron microscope (SEM) images and CFD simulations numerical analysis of stents reflects the interaction of encrustation and flow dynamics for each model. The objective of this study is to identify which ureteral stent design offers the most favorable flow dynamics and the lowest risk of encrustation under standardized, clinically relevant conditions, thereby supporting clinicians in selecting optimal stents for patients with ureteral stenosis. Thereby, the results of this study help clinicians choose the best ureteral stent for patients with ureteral stenosis.

Methods

Modeling of in vitro bladder

The bladder model is a complete closed-drainage system that resembles the urinary bladder[14]. In our current experiment, we have designed a bladder using acrylic with a static volume of 420 mL with an inlet and outlet representing the geometry of the human bladder, as shown in Fig. 1. The in vitro model was carefully designed to reflect key physiological conditions relevant to clinical scenarios with parameters of human body temperature (37 °C), typical urine pH, standard urine ion composition, and the degree of ureteral stenosis incorporated to simulate a realistic environment.

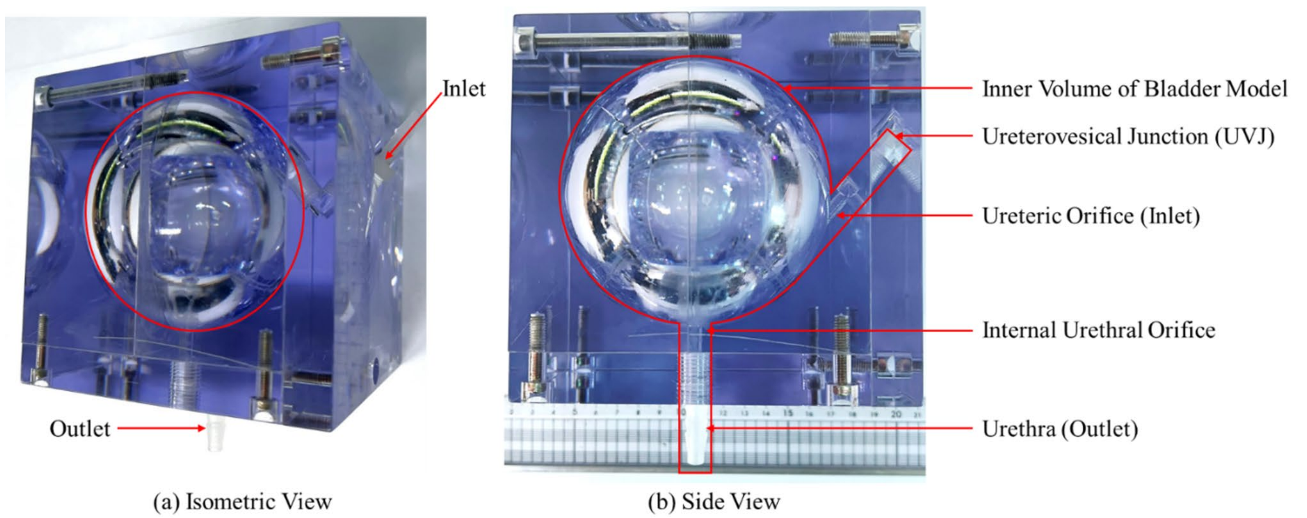

Fig. 1. Acrylic Bladder Model shows the (**a**) Isometric 3D view showing the inlet and outlet and (**b**) Front side view indicating the overall in-vitro components.

Experimental in vitro urinary tract model

Figure 2 illustrates the In Vitro urinary tract model setup, which provides a controlled environment for ureteral stent performance evaluation by simulating the human urinary system. Throughout the studies, a magnetic stirrer operating at 150 RPM keeps the AU moving continuously in a 2-liter reservoir tank to ensure consistent fluid characteristics. The three-headed peristaltic pump that drives the AU through the system replicates the motions that occur naturally in the urinary tract. Urine simulation starts when this pump feeds the AU into a separate in vitro kidney model, which is a box-shaped chamber featuring a flat inlet on the top and a curved outlet at the bottom. The model has an approximate internal volume of 70 mL, an estimated inner surface area of 100 cm^2, and is designed to maintain a baseline flow rate of 60 mL/hr to replicate physiological urine transport conditions.

Following that, the AU passes via silicon ureter tubes, which are 4.57 mm in diameter and roughly resemble the constricted passageways found in human ureters. A 420 ml in vitro bladder model that replicates the bladder's storage function is used in our in vitro system[14]. The AU is collected in a dedicated tank going through the stents and bladder model. As the bladder filled, a valve system was employed to periodically release the accumulated AU, simulating bladder voiding. This extensive setup makes it possible to observe and analyze ureteral stent dynamics and effectiveness in detail under settings that closely resemble those seen in the human urinary system. A potential limitation of the model is the presence of residual air volume within the bladder chamber, which may introduce variability in gas-liquid interactions and influence the crystallization or encrustation dynamics observed during testing.

Ureteral stents selection for the current study

We experimented with three types of ureteral stents as specified in Table 1. CDJS is the most common shape that is used by clinicians and the idea of RDJS is taken from previous research, where RDJS contains 44 side holes compared to 32 in the CDJS, which is expected to allow for improved urine drainage and more effective pressure reduction along a stent of the same length[27]. Alongside the innovative single J stent (SJS) is taken from the pigtail suture stent that was pioneered by Majdalany et al.[32].

To fabricate the stents, we collaborated with the SMG-SNU Boramae Medical Center in Seoul, Korea. The CDJS and RDJS were manufactured at Sungwon Medical Co., Ltd. in Cheongju, Korea, while the SJS was custom-made in our laboratory by cutting the CDJS in half and using the upper portion to create a single J-shaped

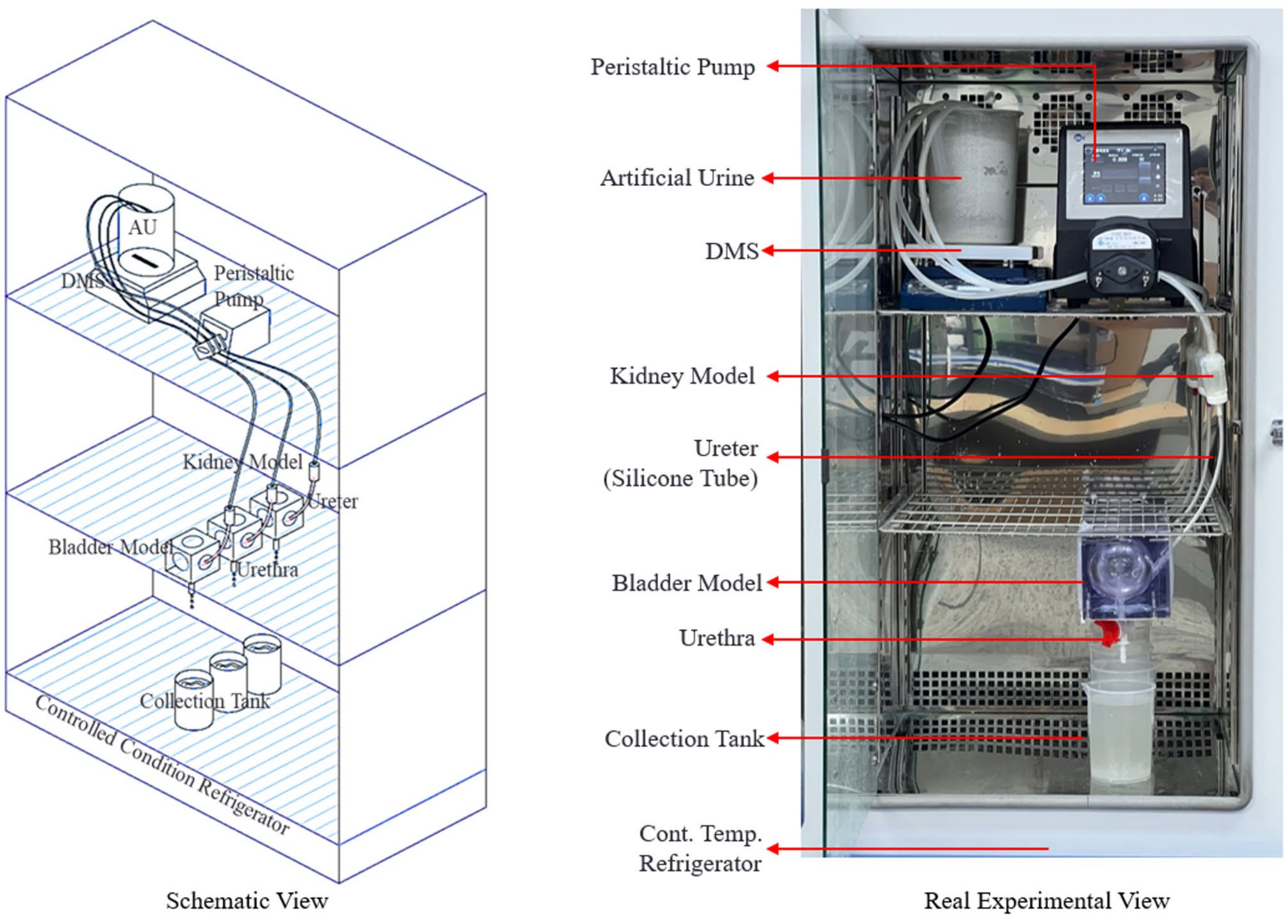

Fig. 2. In Vitro Experimental Setup.

Name of the Ureteral Stent	Length (mm)	Diameter (mm)	Stent Size	Number of Side Holes	Angular Rotation of Side Hole
Conventional Double J Stent (CDJS)	226	4.57	6 Fr	32	90°
Renovated Double J Stent (RDJS)	226	4.57	6 Fr	44	90°
Single J Stent (SJS)	113	4.57	6 Fr	18	90°

Table 1. Specifications of three types of ureteral stents.

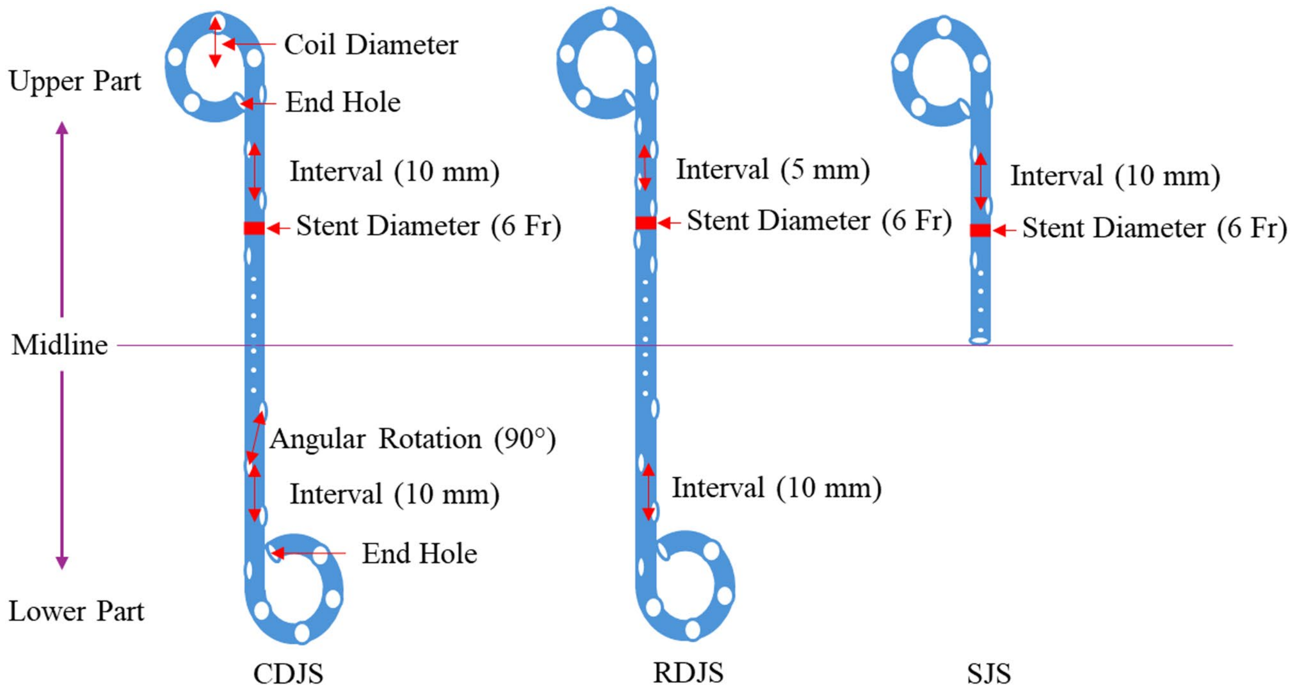

Fig. 3. Geometry of ureteral stents.

structure shown in Fig. 3 and a total of 5 models for each case were used in the experiment. This approach allowed for direct comparison of performance across different stent designs under standardized conditions.

All three stent designs were tested under conditions simulating 50% stenosis near the kidney as shown in Fig. 4.

Stenosis, a narrowing of the ureter, is a common complication in many urological disorders and can significantly affect stent performance, making this simulation highly relevant for clinical applications, and in our experiment, stenosis was applied before stent insertion to better simulate clinical conditions. The degree of ureteral stenosis on the cross-section was defined as

$$\frac{Area\ no\ stenosis - Area\ in\ stenosis}{Area\ no\ stenosis} \times 100\% \tag{1}$$

Experimental process and conditions

The in vitro experimental process is outlined in Fig. 5. The procedure begins with preparing artificial urine stored in a reservoir tank.

The AU is mixed using a magnetic stirrer at 150 RPM to ensure homogeneity. A peristaltic pump controls the flow rate of AU as it enters an in vitro kidney model, mimicking physiological conditions. The AU then flows through silicone ureter tubes containing a stent, maintaining continuous flow for 21 days. After that, the stent is extracted, where we used a careful stent removal method by slicing the silicone ureter to avoid mechanical pulling, some encrustation may still have been dislodged during removal, possibly leading to underestimation, and we have acknowledged this as a limitation. Specifically, all stents were dried at 37 °C for three days to ensure complete removal of residual fluid before weighing. And the stent is considered for analysis, which includes measuring stent mass by Mettler Toledo ML203 precision balance with a resolution of 0.001 g was used to measure stent mass accurately, and examining surface characteristics was done using scanning electron microscopy (SEM). Adhering to the parameters listed in Table 2 created an experimental setting that closely resembled physiological conditions.

To mimic the core temperature of the human body, the temperature was kept at 37 °C. Following the normal urine production of humans, the urine flow rate was fixed at 60 ml/hr. Furthermore, the size of the stents employed was 6 Fr, which is a typical diameter for ureteral stents in clinical use. To simulate slightly alkaline urine, which is

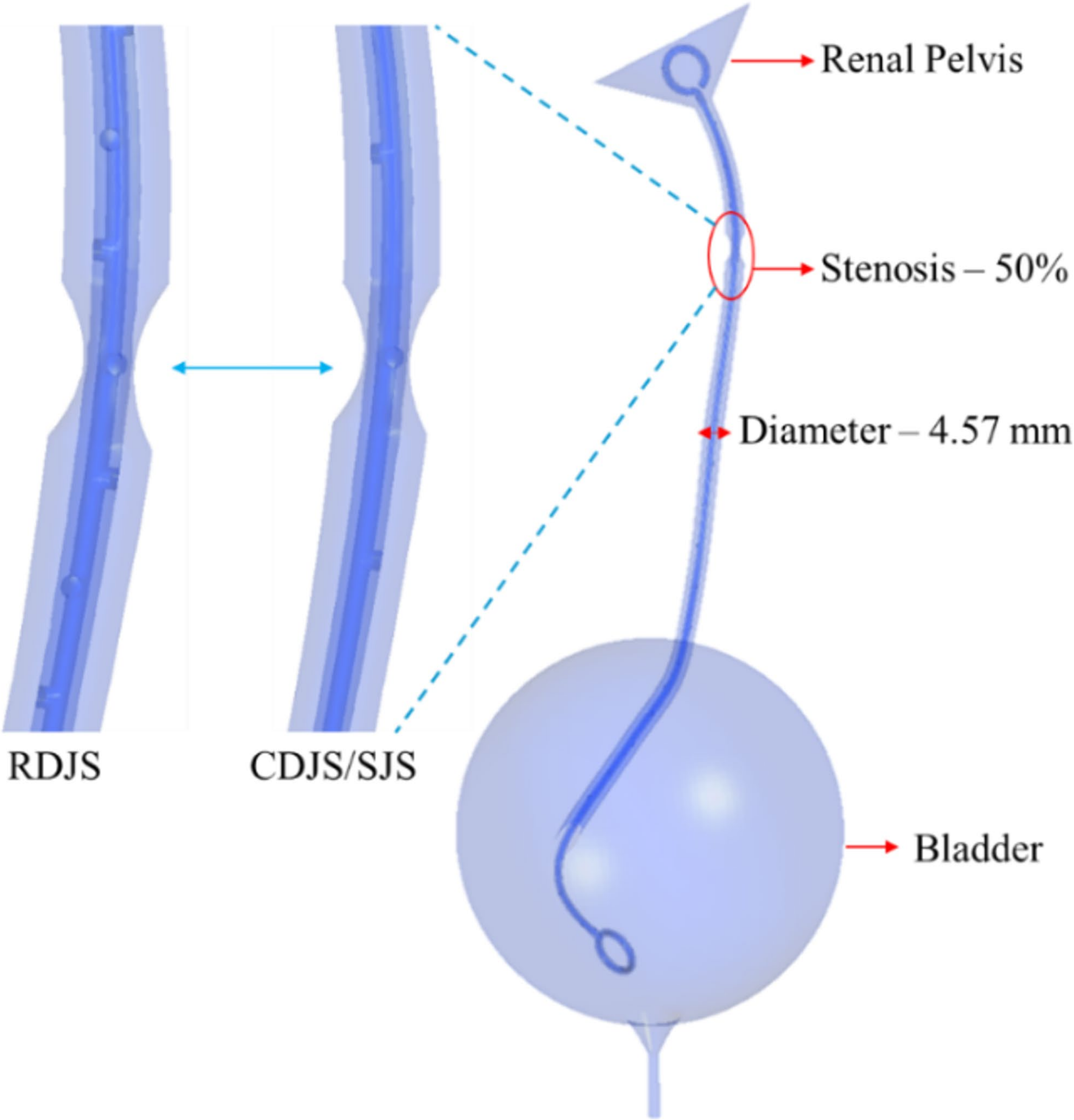

Fig. 4. Indication of Stenosis in the Ureter.

known to affect encrustation formation, a pH of 7.8 was selected. Additionally, to assess the stents' performance in obstructive conditions, which are frequently present in patients who need stent placement, a 50% stenosis rate close to the kidney was used.

Artificial urine composition

A certain composition was used to create artificial urine for this study to resemble human urine closely and the formulation process is shown in Fig. 6. To duplicate the contents of natural urine as indicated in the mass fraction for 1 L of urine in Table 3, the solution was mainly composed of 95% water[33].

Urea ($CO(NH_2)_2$), the main organic compound in urine, was added to simulate the breakdown product of proteins in the human body. Sodium chloride (NaCl) and sodium bicarbonate ($NaHCO_3$) were incorporated to maintain ionic balance and buffer the pH, while sodium sulfate decahydrate ($Na_2SO_4{\cdot}10H_2O$) was included to replicate sulfate excretion.

Furthermore, to replicate the natural content of urine, ammonium chloride (NH_4Cl) and potassium dihydrogen phosphate (KH_2PO_4) were introduced in small proportions. Magnesium sulfate heptahydrate

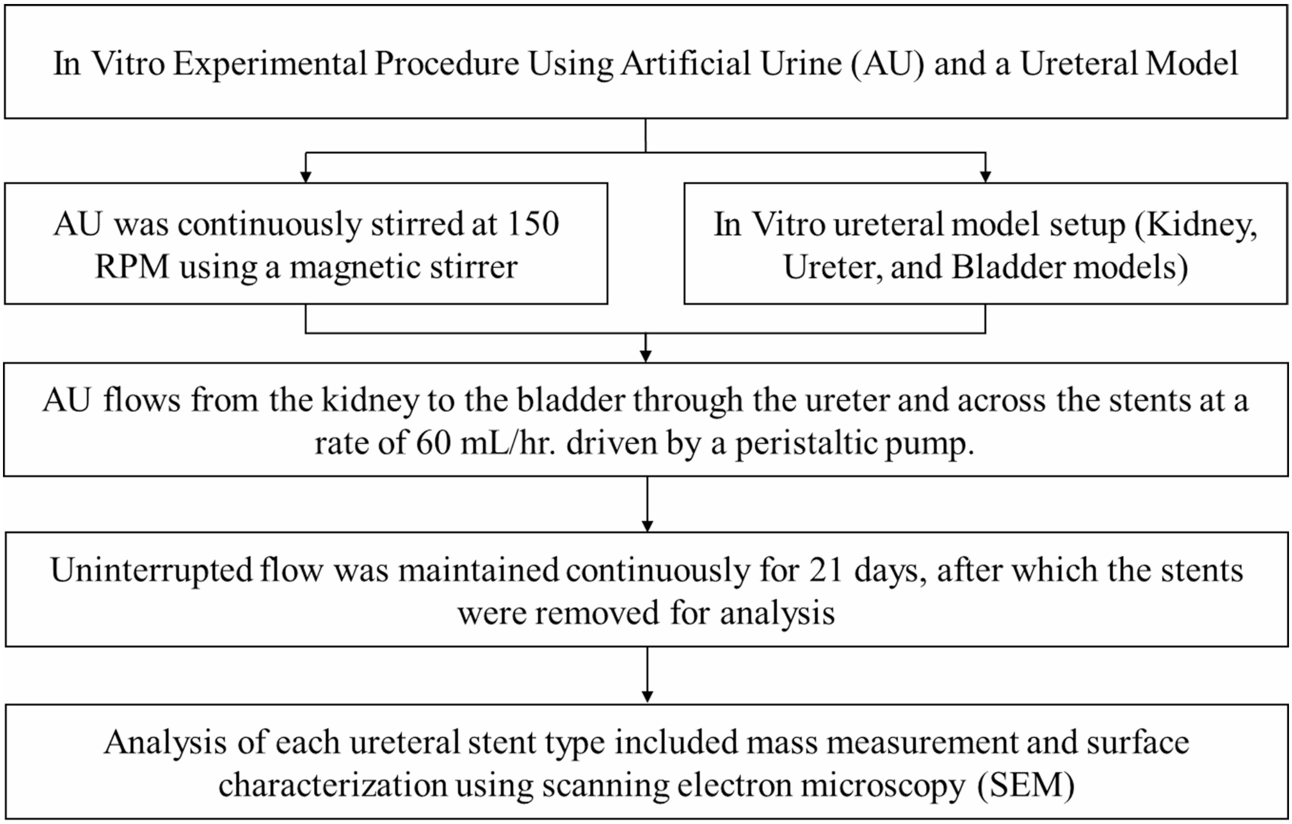

Fig. 5. Block Flow Diagram of Experimental Process.

Parameters	Values
Temperature	37 °C
pH	7.8
Urine Flow	60 mL/hr
Stenosis %	50
Stent Size	6 Fr

Table 2. Experimental parameters.

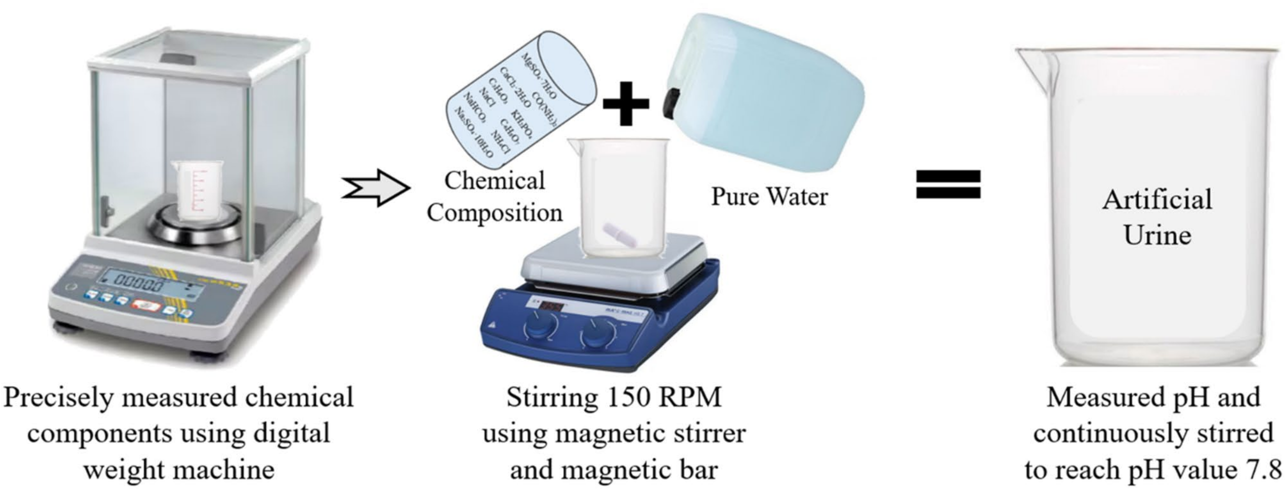

Fig. 6. Preparation of Artificial Urine.

Components	Mass Fraction (1 L-AU)
Water (H_2O)	9.50×10^{-1}
Urea ($CO(NH_2)_2$)	2.26×10^{-2}
Sodium chloride (NaCl)	1.16×10^{-2}
Sodium bicarbonate ($NaHCO_3$)	4.64×10^{-3}
Sodium sulfate decahydrate ($Na_2SO_4 \cdot 10H_2O$)	3.14×10^{-3}
Ammonium chloride (NH_4Cl)	2.95×10^{-3}
Potassium dihydrogen phosphate (KH_2PO_4)	2.11×10^{-3}
Magnesium sulfate heptahydrate ($MgSO_4 \cdot 7H_2O$)	1.09×10^{-3}
Citric acid ($C_6H_8O_7$)	8.50×10^{-4}
Calcium chloride dihydrate ($CaCl_2 \cdot 2H_2O$)	8.10×10^{-4}
Lactic acid ($C_3H_6O_2$)	2.20×10^{-4}

Table 3. Mass fraction of chemical components of artificial urine used in our experiment.

($MgSO_4 \cdot 7H_2O$), citric acid ($C_6H_8O_7$), and calcium chloride dihydrate ($CaCl_2 \cdot 2H_2O$) were also initiated in small proportions to simulate the anti-encrustation and ionic balance functions of these components. Lactic acid was added to simulate organic acids in urine.

Governing equations for fluid flow and numerical simulation

Ansys CFX (ANSYS Inc., USA) 2023R2 was used to investigate the flow phenomenon in the ureter. Since the urine is composed majority of water, the urine employed in numerical simulation has a density and dynamic viscosity comparable to that of water. The dynamic viscosity and density of urine are 0.8583 mPa·s and 1,035 kg/m^3, respectively at a temperature of 37 °C[27]. Urine is regarded as a non-compressible, Newtonian fluid because viscosity varies with temperature which is negligible within the range of 37 °C. The controlled rate urine flow velocity was used for the inlet boundary condition here (60 mL/hr) and outlet (0 Pa) was specified according to the reference study[34]. Ansys ICEM was used for mesh generation. The inlet flow of 60 mL/hr was chosen based on physiological urine production rates, and the 0 Pa outlet condition reflects a free drainage scenario, which is explicitly linked to the clinical relevance of this study. The scale factor and seed size of the ureter models were identical. The stents' ports and side holes were made of prism and tetrahedron meshes. The meshing area shrank as the number of side holes increased.

Results

Analysis of flow rate in ureteral stents

We have analyzed the flow performance for 50% stenosis near the Kidney part, and we found that the flow rate is in a continuous decrease from the first day to the last day. Figure 7 presents an in vitro analysis of flow rate for three stent types: CDJS, RDJS, and SJS for a total of 5 tests per stent type. The box plot illustrates that RDJS has the highest and most consistent flow rate, making it the best-performing stent, while CDJS has the lowest and most variable flow rate. The SJS stent exhibits comparatively low variability and a modest flow rate. The statistical significance of the variations in flow rates among the stent types is confirmed by the highly significant p-values (4.7654e-14 and 3.1146e-09). These results emphasize how crucial it is to comprehend stent performance since choosing stents with better flow characteristics can aid clinicians in improving patient outcomes.

Experimental analysis of stent mass

Figure 8 illustrates the increase in mass for each stent type over 21 days which has been calculated after averaging the initial mass just before starting the experiment, and the final mass after finishing the experiment in our in vitro setup and calculating the rise in the mass of the stents of a total of 5 sets of experiments. Among the three stents, CDJS exhibits the highest values across all metrics with an initial mass of 1.177 g, a final mass of 1.234 g, and an increase in mass of 0.057 g. RDJS follows closely with an initial mass of 1.033 g, a final mass of 1.086 g, and a slightly smaller mass increase of 0.053 g. In contrast, SJS has the lowest values, starting with an initial mass of 0.508 g, a final mass of 0.534 g, and an increase in mass of only 0.025 g.

The variation in mass increase across the five trials was calculated and is presented as standard deviation (SD) in the revised manuscript and shown in Table 4.

This trend highlights that all three types of stents show a positive increase in mass for the same input conditions. SJS might be preferable for short-term use in cases where reducing encrustation risk is critical compared to RDJS and CDJS, though stent selection in clinical practice should consider individual factors such as ureter length, curvature, and mobility to ensure proper placement and function.

Visualization of encrustation formation

Each type of stent's raw pictures on the 1st day of the experiment and after 21 days are displayed in Fig. 9. Visually, the variations in encrustation development and surface roughness are noticeable. After 21 days, the RDJS and CDJS exhibit more obvious encrustation, whereas the SJS keeps its surface comparatively fresh.

The SEM pictures of the stents at different magnifications (1 mm, 20 µm, and 10 µm) are displayed in Fig. 10, which demonstrates clear encrustation patterns on the stent surfaces. The most severe encrustation is seen in CDJS, which may cause obstruction and reduced urine flow because of its massive, dense calcified deposits and

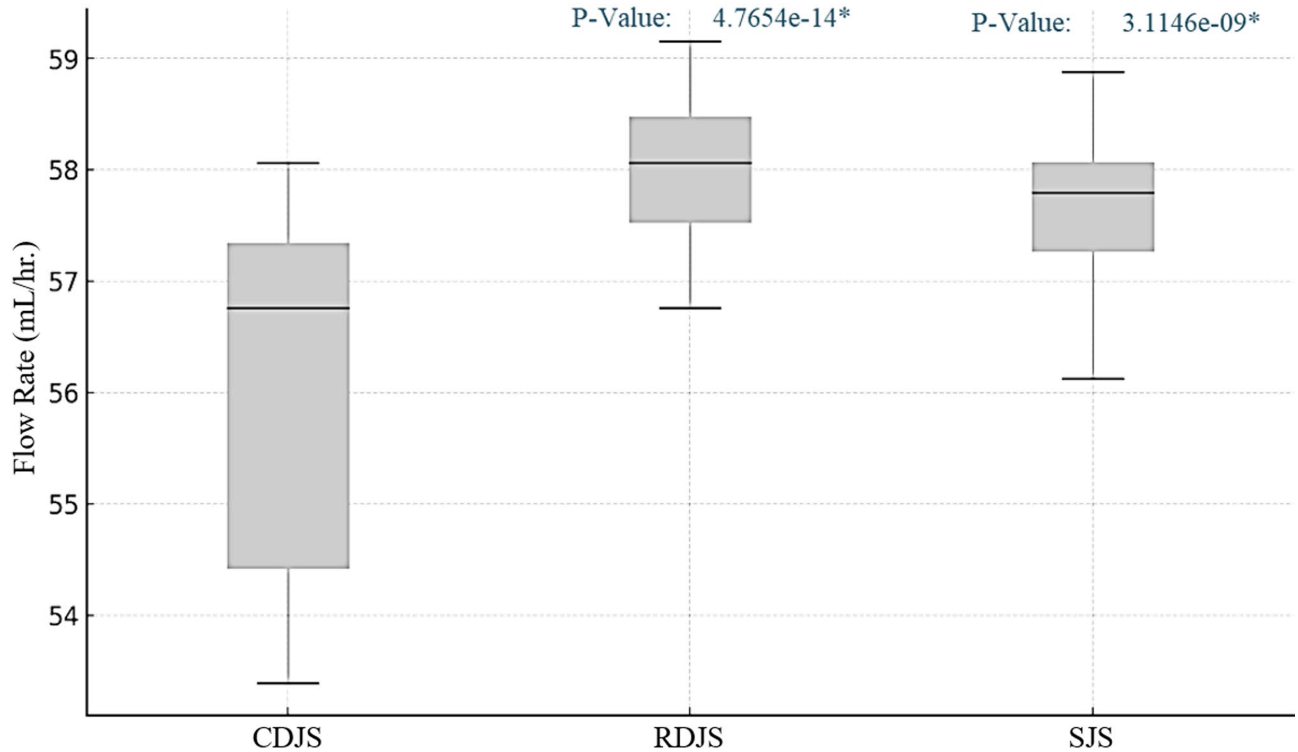

Fig. 7. Flow rate of each stent through the experimental period.

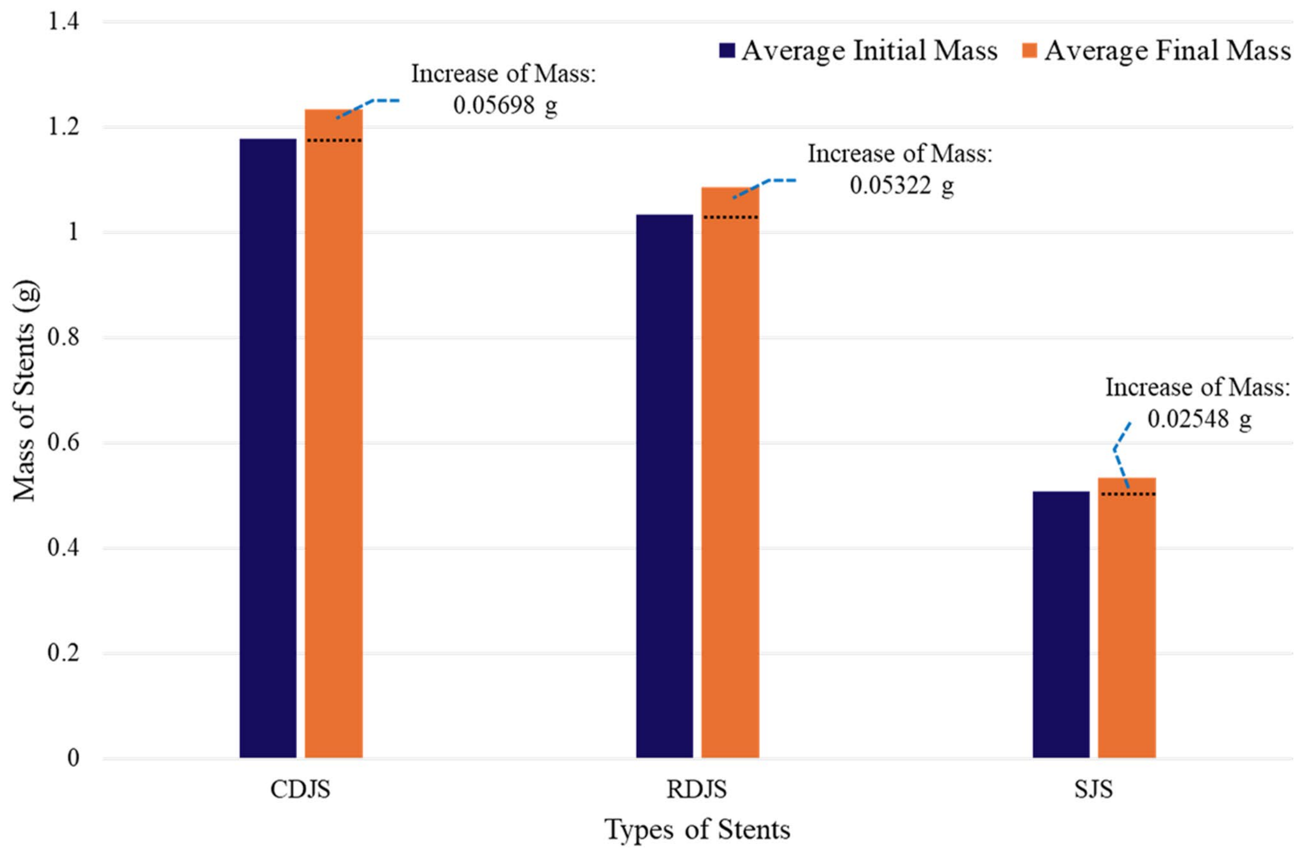

Fig. 8. Mass increase rate at Stents.

Stent Type	Sample 1	Sample 2	Sample 3	Sample 4	Sample 5	Mean ± SD
CDJS	0.061	0.054	0.060	0.056	0.054	0.057 ± 0.006
RDJS	0.057	0.049	0.054	0.051	0.054	0.053 ± 0.005
SJS	0.028	0.023	0.026	0.024	0.025	0.025 ± 0.003

Table 4. Individual mass increase (g) of ureteral stents across five experiments.

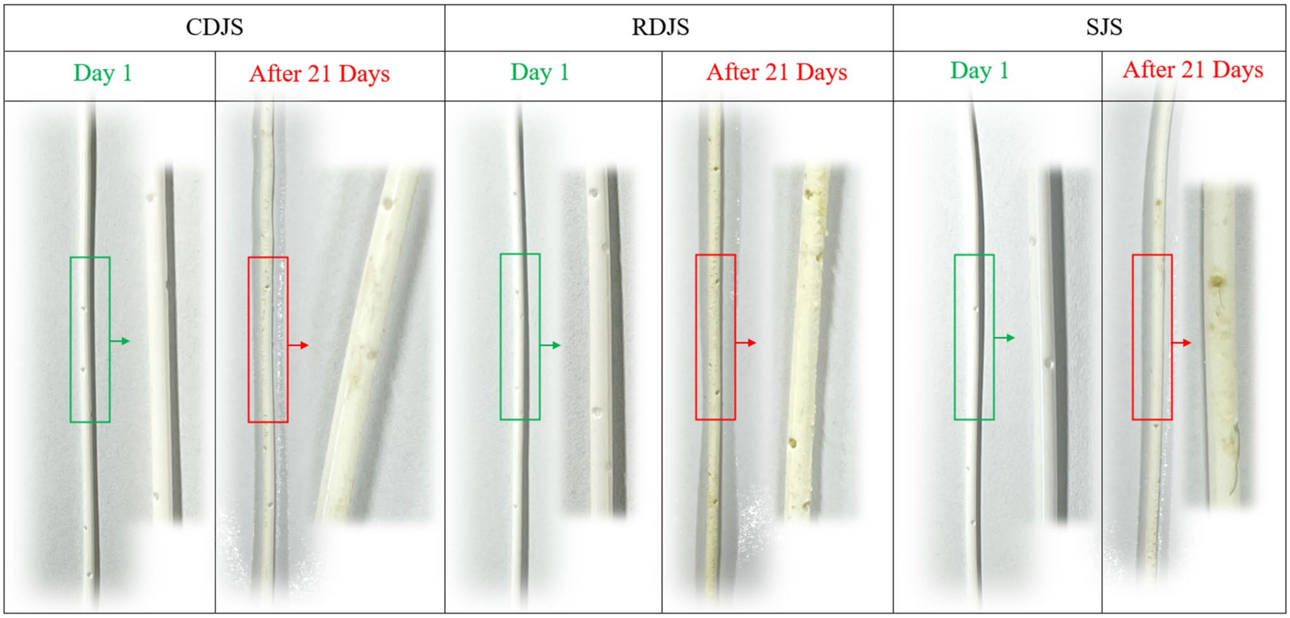

Fig. 9. Surface Visualization of Stents.

crystalline formations. With uneven crystal forms and dispersed deposits, RDJS exhibits mild encrustation, indicating marginally improved performance. The SJS with a comparatively smooth surface and tiny consistent deposits exhibits less encrustation and a lower risk of issues connected to encrustation. According to surface area analysis from SEM results, it is analyzed that about 10.37% of the surface area was covered in encrustation for SJS, 13.04% for RDJS, and 13.52% for CDJS close to the side holes. Specifically, lower surface coverage (10.37%) implies a reduced likelihood of early stent occlusion, which is particularly beneficial in high-risk patients or those requiring short-term stent placement. In contrast, higher coverage observed in CDJS (13.52%) accelerates encrustation buildup, potentially leading to increased urinary flow resistance, patient discomfort, and earlier stent failure, while RDJS is more suitable than CDJS. These findings suggest that SJS is preferable in clinical implications.

Following the visualization of Fig. 10, the inside and outside of the stents' side hole areas, where the encrusted particles are marked in Fig. 11.

Table 5 outlines the rate of the encrusted area around the stenosis side holes and the average size of particles, which have been calculated from the SEM images. Statistical comparison of encrusted surface area percentages revealed significantly lower encrustation in RDJS compared to CDJS ($p = 0.004$) for the outer surface of the side hole. Particle sizes were also significantly smaller in SJS and RDJS compared to CDJS ($p = 0.013$ and 0.021, respectively.

Analysis of CFD results

Wall shear stress (WSS)

Wall Shear Stress (WSS) magnitudes ranging from 0 Pa to 12 mPa are seen in CFD results in Fig. 12, with areas of strong WSS located close to narrowing sections, especially at the stenosis hole. This figure uses labeled regions and 3D visuals to compare three stents and show their WSS distributions. In contrast to the global constriction used in the in vitro ureter model, the CFD simulations incorporated a localized stenosis near the upper ureter to enable high-resolution analysis of wall shear stress and flow behavior around the stenotic region, where encrustation is typically most pronounced. This modeling strategy allowed for more precise evaluation of side-hole flow dynamics and stress concentrations relevant to encrustation risk.

WSS data for SJS at the stenosis hole displayed values as high as 10.4 mPa which is quite below in comparison to Mosayebbi et al.'s maximum of 15 mPa[35] and this study's contrasted with the study's range (0.01 ~ 1.02 mPa) to Zheng et al. (0.49 ~ 2.80 mPa)[26] in the WSS result comparison section. Streamlines and close-up views highlight important areas of high WSS, identifying important stress concentrations adjacent to SH and confirming the

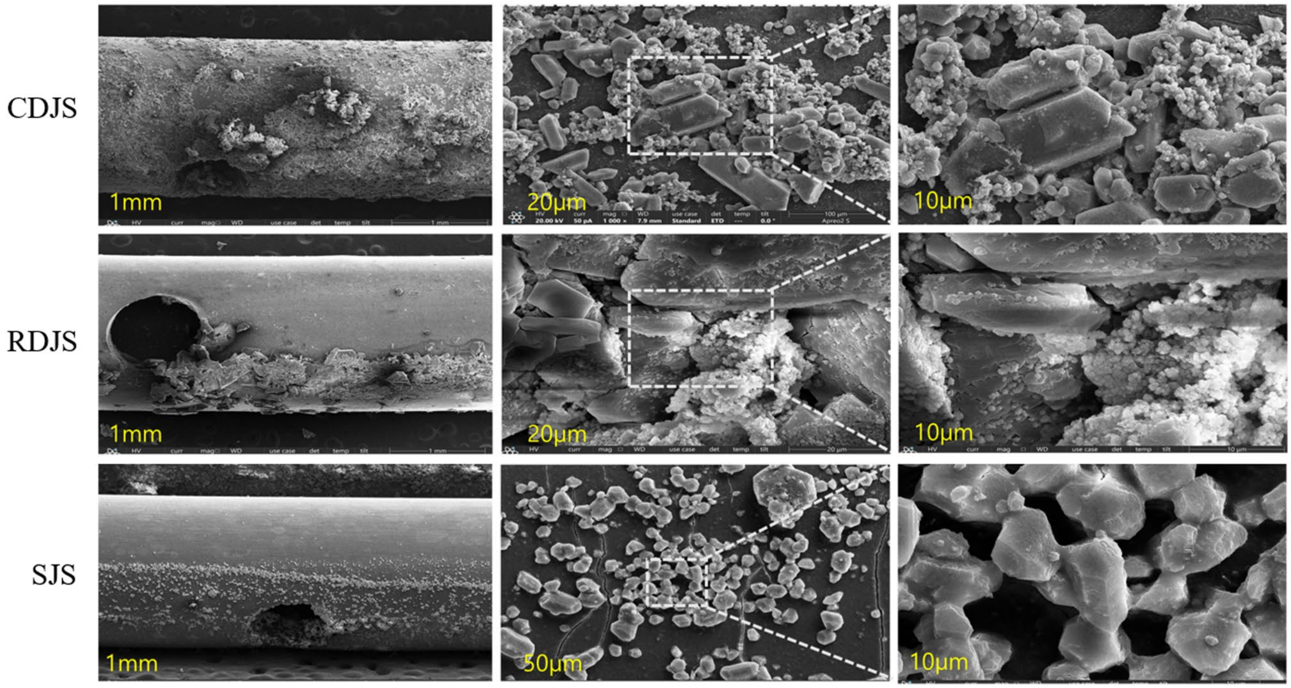

Fig. 10. SEM images of the Stents.

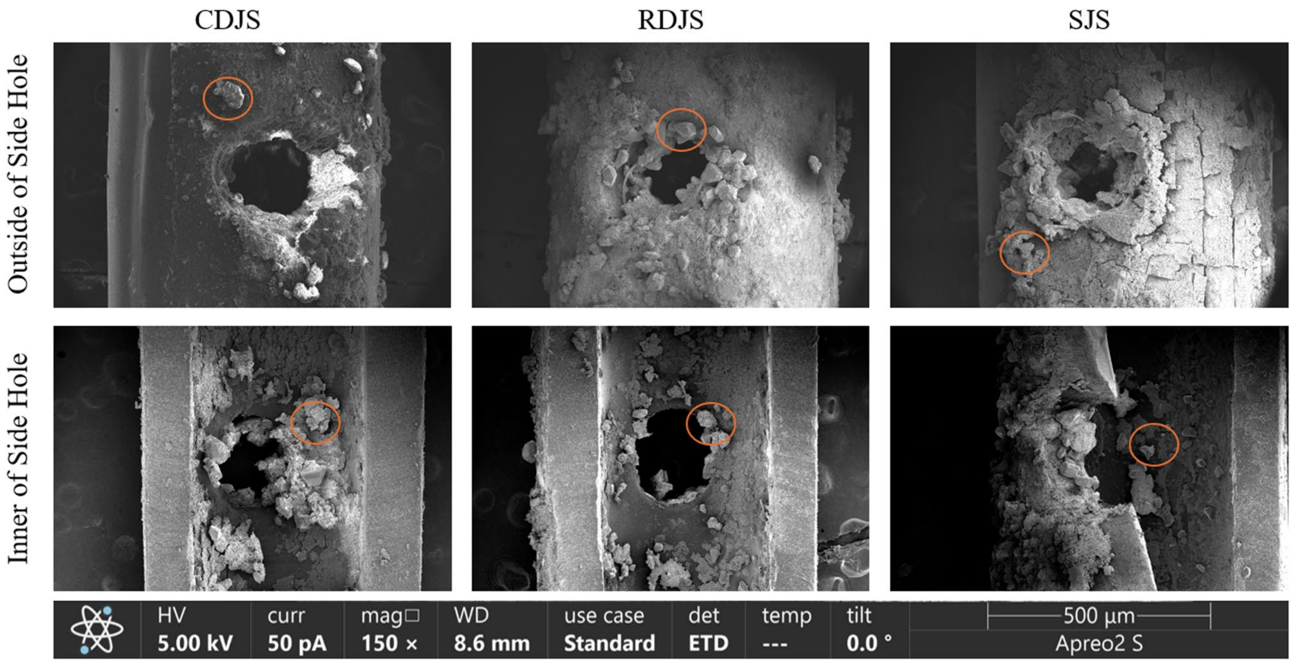

Fig. 11. Visualization of the outside and inner surface of the stent hole by SEM images.

results of the current study with previous research. Furthermore, Fig. 13 illustrates the WSS distribution along three distinct ureteral types and connects it to encrustation patterns using SEM and raw stent images. These CFD results align closely with experimental observations. SJS exhibited the highest WSS near the stenosis hole (10.4 mPa), which corresponds with the lowest encrustation surface area (10.37%) and the smallest mass increase (0.025 g). In contrast, CDJS showed the lowest WSS in this region, consistent with its highest encrustation coverage (13.52%) and maximum mass gain (0.057 g).

Stent Types	% of Area Encrusted (Mean ± SD) Outside of the Side Hole	Inner of the Side Hole	Average Size of Particles (μm ± SD)	*p*-value (Outside of the Side Hole)	*p*-value (Inner of the Side Hole)	*p*-value (Average Size of Particles)
CDJS	4.2 ± 0.3	2.1 ± 0.2	5.92 ± 0.4	Ref	Ref	Ref
RDJS	2.2 ± 0.4	1.2 ± 0.3	4.71 ± 0.3	0.004	0.006	0.021
SJS	3.5 ± 0.2	2.0 ± 0.2	4.58 ± 0.2	0.017	0.684	0.013

Table 5. Rate of encrustation around the stent hole at the stenosis area and size of encrustation particles.

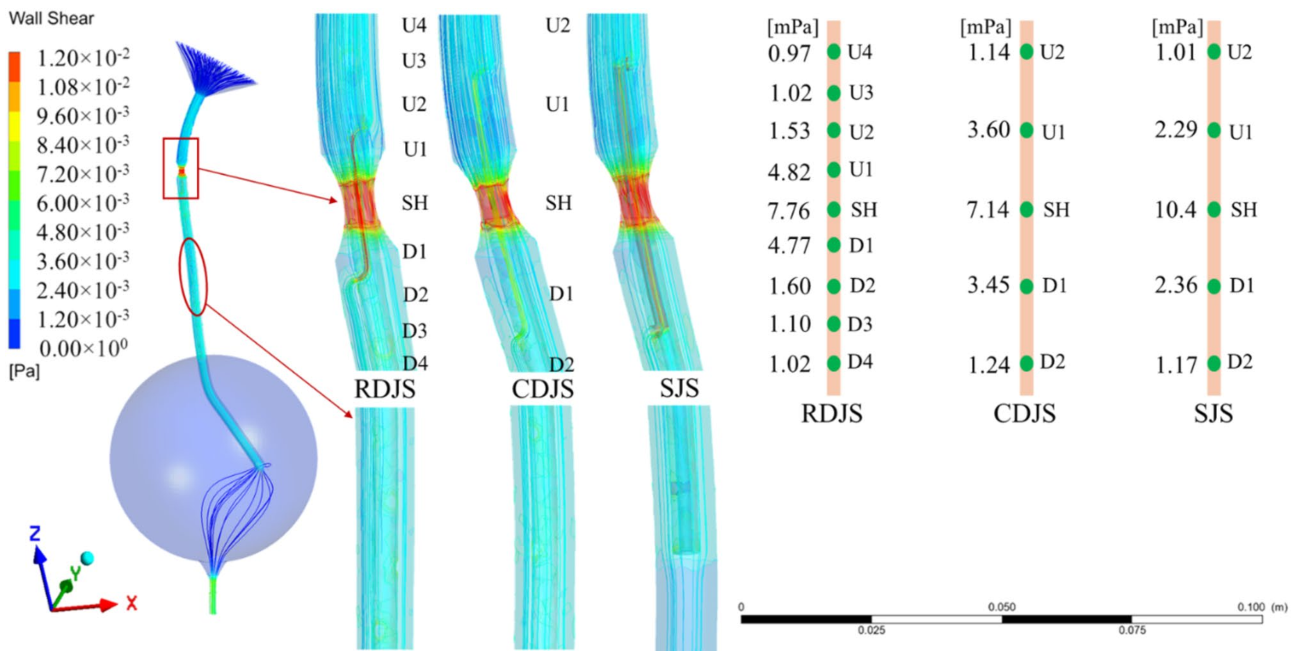

Fig. 12. CFD analysis of wall shear stress.

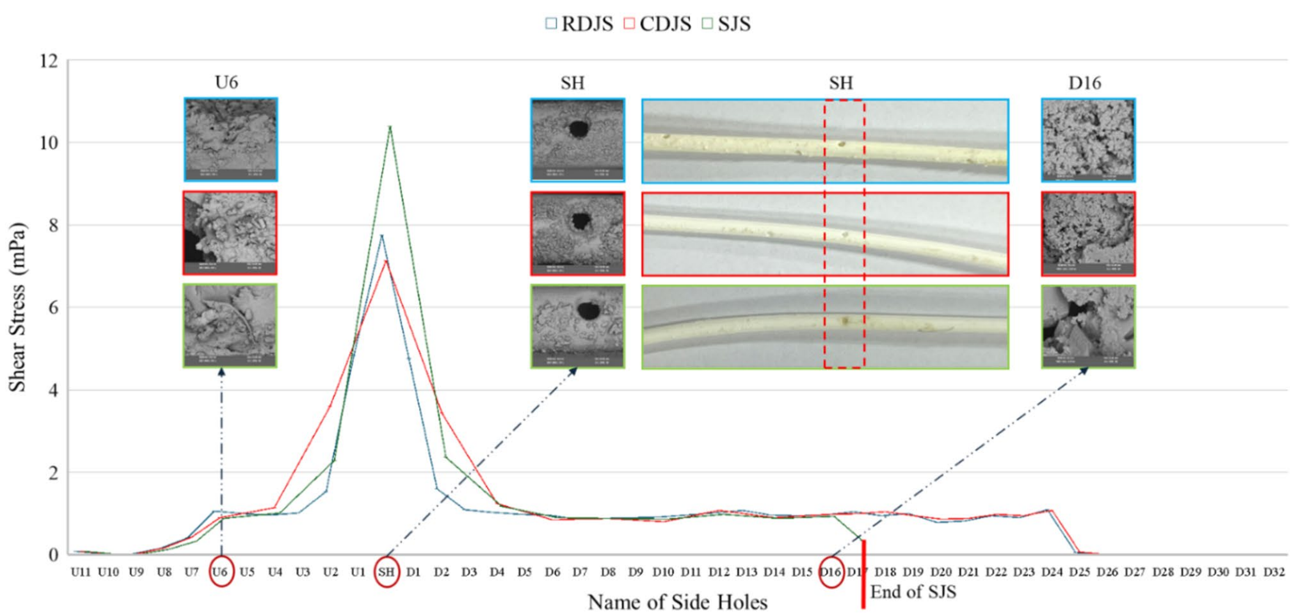

Fig. 13. Comparison of encrustation and wall shear stress.

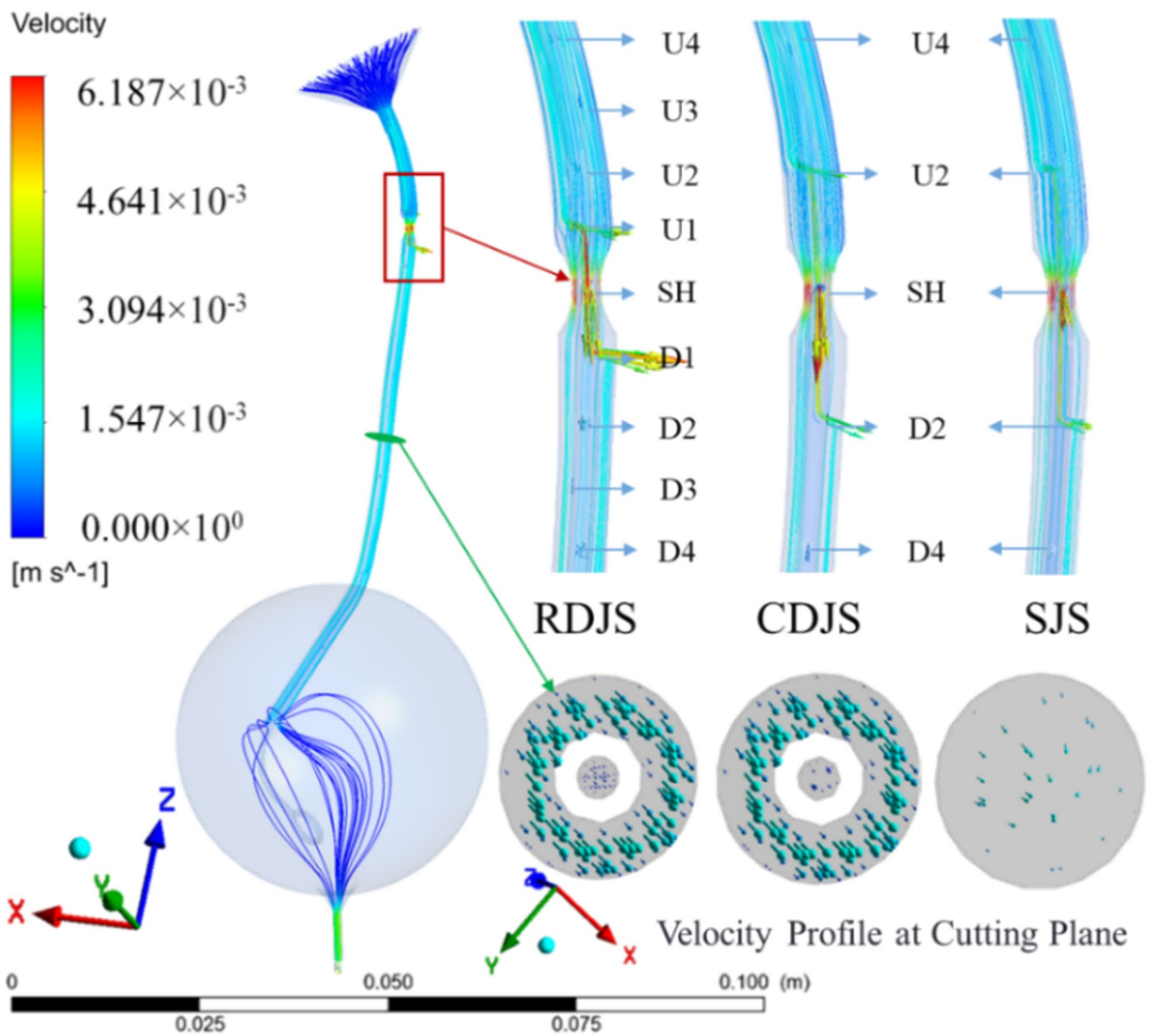

Fig. 14. Velocity profile of the ureteral stents.

The figure analysis shows that SJS consistently exhibits higher WSS than RDJS and CDJS, particularly in the vicinity of the stenosis holes (SH). Consequently, the WSS peaks of SJS display the maximum value. In regions such as U6 and D16, RDJS and CDJS show severe and mild encrustation, respectively.

Velocity profile

Furthermore, simulation of the velocity distribution inside a ureter with a stent is shown in Fig. 14. Both a longitudinal view and cross-sectional cutting planes are used to display the velocity profile. The red box in the main longitudinal image highlights areas of high velocity close to a stenosed region, highlighting streamlines of fluid flow. At the stenosis, the flow dramatically speeds up and shows a higher rate for CDJS and RDJS compared to SJS. As the flow re-expands further downstream, the velocity drops in every stent.

The velocity distribution across the stent lumen at various axial positions is depicted by the cutting planes, which are circular cross-sections. Because of boundary layer effects these profiles show unequal velocity distributions with lower velocities close to the walls and higher velocities clustered around the center.

Discussion

The observed surface visibility and mass increases of all three stent types over 21 days suggest a significant difficulty in the usage of ureteral stents, as demonstrated by the encrustation shown in Figs. 9 and 10, which shows a similar trend to previous research by Arkusz et al.[36] reported comparable surface-level encrustation characteristics after 18 days of stent placement in pediatric patients, highlighting the early onset of mineral deposition patterns near side holes. The mass increase shown in Fig. 8 and the SEM surface analysis in Figs. 9 and 10 showed that the CDJS and RDJS were more susceptible to encrustation than the SJS. The SJS's reduced encrustation rates imply less crystal nucleation and deposition. The RDJS displayed quite good flow performance and comparable amounts of encrustation to the CDJS. This is because the RDJS has more side pores, which not only improve urine flow dispersion but also provide additional locations for crystal attachment[37]. With the shorter length and fewer side holes, the SJS exposed less surface to urine, leaving the surface cleaner after prolonged use, and p-values in SEM-based encrustation analysis in Table 5 support the finding and enhance the robustness of comparative analysis.

The importance of stent selection in preserving sufficient urine flow in stenosed situations is shown by the analysis of in vitro flow rate[38]. The RDJS performed better than the SJS and CDJS in terms of flow uniformity and average flow rates among the three types (Fig. 7). These results are consistent with CFD data, which showed that the RDJS successfully reduced low WSS locations, lowering the possibility of encrustation.

The relationship between stent geometry, flow behavior and encrustation risk was better understood with CFD simulations. Critical areas where low WSS correlated with increased encrustation levels were detected by the WSS distribution over the stent surfaces (Fig. 12). In contrast to the CDJS and RDJS, the SJS showed very uniform WSS distributions with fewer stagnation zones as shown in Fig. 12, which is consistent with the experimental results of less encrustation. Additionally, a thorough understanding of how urine flow affects stent performance was made possible by the integration of in vitro data with CFD models. Encrustation risk in side-hole locations is indicated by the higher WSS values (10.4 mPa) seen in the RDJS close to stenosed regions.

Balance in flow performance and encrustation resistance is crucial in stent selection[39]. From the analysis of WSS in Figs. 12 and 13, SJS with its reduced size and lower encrustation levels offers a viable alternative for patients who need short-term stent insertion or who are more susceptible to encrustation, even if the RDJS performed better in terms of flow rate than the CDJS and SJS as seen from Figs. 9 and 14. Its moderate flow performance, however, indicates that more improvements are required to guarantee effectiveness in situations involving severe obstruction.

Limitations

This study has several limitations that should be considered when interpreting the results. First, the sample size was limited to five stents per type due to the time-intensive nature of the experimental protocol and the daily preparation requirements for artificial urine. While efforts were made to ensure consistency and control, the small sample size may limit the statistical power of the findings. Future studies incorporating larger sample sizes will be essential to improve the robustness and generalizability of the results.

Second, although the artificial urine used in this study was prepared under supersaturated conditions to simulate human urine composition, it did not include urinary proteins or account for patient-specific biochemical and microbiological factors. These components can influence mineral precipitation kinetics and encrustation behavior in vivo and thus represent a limitation of the in vitro model.

Third, the study investigated only a single degree of ureteral stenosis (50%), chosen to represent a clinically relevant obstruction. However, the clinical applicability of the findings could be broadened by evaluating stent performance under a wider range of stenotic conditions in future work.

Lastly, the computational simulations assumed constant viscosity based on water-like properties. Urine viscosity can vary depending on protein content and disease states, which may affect flow behavior and wall shear stress (WSS) predictions. This simplification should be considered when interpreting the CFD results and is acknowledged as a limitation of the numerical model.

Conclusion

Combining in vitro examinations with CFD simulations, this study provides a comprehensive evaluation of encrustation formation and flow performance for three different ureteral stent types. Important variables that determine stent performance like wall shear stress distribution, urine flow patterns and encrustation of the surface stents were identified. Among the types of stents analyzed, SJS was found to develop the least amount of encrustation, thus being less likely to block the urethra and function better in the long term. Based on the number of side holes RDJS was found to have the highest flow performance, while CDJS had the greatest incidence of encrustation which impaired its urine flow. These performance in vitro findings were captured in CFD results which illustrated that SJS developed significantly less encrustation while exhibiting higher WSS. Based on the findings, we recommend that the Single J Stent (SJS) be considered for short-term use in patients who are at high risk of encrustation or those requiring temporary drainage following procedures. Its shorter length and lower surface area resulted in reduced encrustation and may help lower the risk of stent-related complications during short indwelling periods. Conversely, the Renovated Double J Stent (RDJS), which demonstrated the most stable and highest flow rate performance, may be more suitable for patients requiring long-term stenting, especially in obstructed ureters. These insights can help guide personalized stent selection to improve patient outcomes and reduce the need for early stent replacement due to complications such as blockage or infection.

Data availability

The datasets used and/or analyzed during the current study are available from the corresponding author on reasonable request.

Received: 14 March 2025; Accepted: 26 May 2025
Published online: 01 July 2025

References

1. Fiuk, J., Bao, Y., Calleary, J. G., Schwartz, B. F. & Denstedt, J. D. The use of internal stents in chronic ureteral obstruction. *J. Urol.* **193**, 1092–1100. https://doi.org/10.1016/j.juro.2014.10.123 (2015).
2. Mansour, S., El- Meligy, A., Hassan, O. I., Salem, F. E. H. & A. & Effect of educational intervention for nurses about pre and Post-Operative care on clinical outcomes of patients undergoing ureteral stent surgery. *Egypt. J. Health Care*. **11**, 1012–1031. https://doi.org/10.21608/ejhc.2020.225126 (2020).
3. Williams, K. G., Blacker, A. J. & Kumar, P. Ureteric stents: the past, present and future. *J. Clin. Urol.* **11**, 280–284. https://doi.org/10.1177/2051415817722934 (2018).
4. Lange, D., Bidnur, S., Hoag, N. & Chew, B. H. Ureteral stent-associated complications—where we are and where we are going. *Nat. Rev. Urol.* **12**, 17–25. https://doi.org/10.1038/nrurol.2014.340 (2015).
5. Mosayyebi, A., Manes, C., Carugo, D. & Somani, B. K. Advances in ureteral stent design and materials. *Curr. Urol. Rep.* **19**, 1–9. https://doi.org/10.1007/s11934-018-0779-y (2018).
6. Hsiao, C. Y., Chen, T. H., Lee, Y. C. & Wang, M. C. Ureteral stone with hydronephrosis and urolithiasis alone are risk factors for acute kidney injury in patients with urinary tract infection. *Sci. Rep.* **11**, 23333. https://doi.org/10.1038/s41598-021-02647-8 (2021).
7. Guo, H. & Yuan, J. B. New insights into the prevention of ureteral stents encrustation. *Open Med.* https://doi.org/10.1515/med-2023-0854 (2023).
8. Bithelis, G. et al. Assessment of encrustations on polyurethane ureteral stents. *J. Endourol.* **18**, 550–556. https://doi.org/10.1089/end.2004.18.550 (2004).
9. Lee, S. B. et al. Evaluation of encrustation of double J stents with artificial urine. *Clin. Nephrol.* **99**, 290–298. https://doi.org/10.5414/CN111038 (2023).
10. Choong, S. K. & Whitfield, H. N. Urinary encrustation of alloplastic materials. *J. Endourol.* **14**, 19–23. https://doi.org/10.1089/end.2000.14.1 (2000).
11. Mennuni, G. et al. Prevention and treatment of nephrolithiasis: A review on the role of spa therapy. *Clin. Ter.* **166**, 344–356. https://doi.org/10.7417/T.2015.1890 (2015).
12. Heyns, C. F. Urinary tract infection associated with conditions causing urinary tract obstruction and stasis, excluding urolithiasis and neuropathic bladder. *World J. Urol.* **30**, 77–83. https://doi.org/10.1007/s00345-011-0725-9 (2012).
13. Longhurst, P. A. & Uvelius, B. Pharmacological techniques for the in vitro study of the urinary bladder. *J. Pharmacol. Toxicol. Methods*. **45**, 91–108. https://doi.org/10.1016/S1056-8719(01)00133-2 (2001).
14. Milo, S. et al. An in-situ infection detection sensor coating for urinary catheters. *Biosens. Bioelectron.* **81**, 166–172. https://doi.org/10.1016/j.bios.2016.02.059 (2016).
15. Rasouly, H. M. & Lu, W. Lower urinary tract development and disease. *WIREs Syst. Biol. Med.* **5**, 307–342. https://doi.org/10.1002/wsbm.1212 (2013).
16. Abbott, I. J. et al. Fosfomycin efficacy and emergence of resistance among Enterobacteriaceae in an in vitro dynamic bladder infection model. *J. Antimicrob. Chemother.* **73**, 709–719. https://doi.org/10.1093/jac/dkx441 (2018).
17. Rad, H. I. et al. Allicin prevents the formation of Proteus-induced urinary crystals and the blockage of catheter in a bladder model in vitro. *Microb. Pathog.* **132**, 293–301. https://doi.org/10.1016/j.micpath.2019.05.016 (2019).
18. Gaonkar, T. A. et al. Evaluation of the antimicrobial efficacy of urinary catheters impregnated with antiseptics in an in vitro urinary tract model. *Infect. Control Hosp. Epidemiol.* **24**, 506–513. https://doi.org/10.1086/502241 (2003).
19. Xu, Y., Wang, J., Hao, Z., Wang, S. & Liang, C. Biodegradable Ciprofloxacinincorporated waterborne polyurethane polymers prevent bacterial biofilm formation in vitro. *Exp. Ther. Med.* **17**, 1831–1836. https://doi.org/10.3892/etm.2018.7113 (2019).
20. Roberts, A. E., Kragh, K. N., Bjarnsholt, T. & Diggle, S. P. The limitations of in vitro experimentation in Understanding biofilms and chronic infection. *J. Mol. Biol.* **427**, 3646–3661. https://doi.org/10.1016/j.jmb.2015.09.002 (2015).
21. Chua, R. Y. R., Lim, K., Leong, S. S. J., Tambyah, P. A. & Ho, B. An in-vitro urinary catheterization model that approximates clinical conditions for evaluation of innovations to prevent catheter-associated urinary tract infections. *J. Hosp. Infect.* **97**, 66–73. https://doi.org/10.1016/j.jhin.2017.05.006 (2017).
22. Cox, A. J., Hukins, D. W. L., Davies, K. E., Irlam, J. C. & Sutton, T. M. An automated technique for in vitro assessment of the susceptibility of urinary catheter materials to encrustation. *Eng. Med.* **16**, 37–41. https://doi.org/10.1243/EMED_JOUR_1987_016_009_02 (1987).
23. Pannek, J. et al. An in-vitro model for bacteria-related catheter encrustations. *World J. Urol.* **42**, 469. https://doi.org/10.1007/s00345-024-05191-y (2024).
24. Agarwal, J. & Radera, S. Biofilm-mediated urinary tract infections. In Biofilms in Human Diseases: Treatment and Control (ed (eds Kumar, S. et al.) (Springer, Cham, https://doi.org/10.1007/978-3-030-30757-8_13 (2019).
25. Hu, J. et al. In vitro and in vivo assessment of a bilayered degradable rapamycin-eluting stent for ureteral stricture caused by holmium: YAG laser lithotripsy. *Acta Biomater.* **172**, 321–329. https://doi.org/10.1016/j.actbio.2023.10.009 (2023).
26. Zheng, S. et al. Fluid mechanical performance of ureteral stents: the role of side hole and lumen size. *Bioeng. Transl Med.* **1**, 1. https://doi.org/10.1002/btm2.10407 (2022).
27. Choi, Y. H. et al. Evaluation of renovated double J stents using ureter models with and without stenosis. *World J. Urol.* **42**, 228. https://doi.org/10.1007/s00345-024-04920-7 (2024).
28. Shilo, Y. et al. Comparative study of renal drainage with different ureteral stents subject to extrinsic ureteral obstruction using an in vitro ureter-stent model. *BMC Urol.* **21**, 1–8. https://doi.org/10.1186/s12894-021-00865-w (2021).
29. Zheng, S. et al. Fluid mechanical modeling of the upper urinary tract. *WIREs Mech. Dis.* **13**, e1523. https://doi.org/10.1002/wsbm.1523 (2021).
30. Mosayyebi, A. et al. The accumulation of particles in ureteric stents is mediated by flow dynamics: full-scale computational and experimental modeling of the occluded and unoccluded ureter. *APL Bioeng.* **6**, 026102. https://doi.org/10.1063/5.0083260 (2022).
31. Vogt, B. Investigating the encrustation of reinforced ureteral stents by computational flow dynamic simulations. *World J. Urol.* **41**, 1451–1457. https://doi.org/10.1007/s00345-023-04356-5 (2023).
32. Majdalany, S. E. et al. In vivo evaluation of a novel Pigtail suture stent. *Urology* https://doi.org/10.1016/j.urology.2020.11.031 (2020).
33. Mosayyebi, A. Mechanisms of encrustation within ureteral stents. Doctoral Thesis, University of Southampton (2018).
34. Kim, K. W. et al. Analysis of urine flow in three different ureter models. *Comput. Math. Methods Med.* **11**, 5172641. https://doi.org/10.1155/2017/5172641 (2017).
35. Mosayyebi, A. et al. Reducing deposition of encrustation in ureteric stents by changing the stent architecture: A microfluidic-based investigation. *Biomicrofluidics* **13**, 014101. https://doi.org/10.1063/1.5059370 (2019).
36. Arkusz, K. et al. Surface analysis of ureteral stent before and after implantation in the bodies of child patients. *Urolithiasis* **49**, 83–92. https://doi.org/10.1007/s00240-020-01211-9 (2021).
37. Vladkova, T. G. et al. Surface engineered biomaterials and ureteral stents inhibiting biofilm formation and encrustation. *Surf. Coat. Technol.* **404**, 126424. https://doi.org/10.1016/j.surfcoat.2020.126424 (2020).
38. Kim, K. W. et al. Urine flow analysis using double J stents of various sizes in in vitro ureter models. *Int. J. Numer. Methods Biomed. Eng.* **36**, e3294. https://doi.org/10.1002/cnm.3294 (2020).
39. Liu, S. et al. Enhanced long-term performance of ureteral stents with functional coating: combating bacterial adhesion and inhibiting encrustation. *Prog Org. Coat.* **192**, 108512. https://doi.org/10.1016/j.porgcoat.2024.108512 (2024).

Acknowledgements
This work was supported by the National Research Foundation of Korea (NRF) grant funded by the Korea government (MSIT) (2021R1F1A1051004). This work was also supported by the Glocal University 30 Project Fund of Gyeongsang National University in 2025.

Author contributions
Md. Didarul Islam: Conceptualization (equal), Data curation (lead), Formal analysis (lead), Investigation (lead), Methodology (lead), Software (lead), Validation (equal), Writing-Original draft (lead). Hyo Jeong Kang: Investigation (equal), Methodology (equal), Software (equal), Validation (equal). Sung Jin Tae: Data curation (supporting), Investigation (supporting), Methodology (supporting), Software (supporting). Kyung-Wuk Kim: Methodology (supporting), Software (equal). Young Ho Choi: Methodology (equal), Software (supporting), Validation (supporting). Seung Bae Lee: Methodology (supporting), Writing- reviewing and editing (supporting). Md Rakibuzzaman: Software (supporting), Validation (supporting). Min Uk Kim: Conceptualization (equal), Methodology (equal), Supervision (equal), Writing- reviewing and editing (equal). Hyoung-Ho Kim: Conceptualization (lead), Methodology (equal), Software (equal), Supervision (lead), Validation (equal), Writing- reviewing and editing (lead).

Declarations

Competing interests
The authors declare no competing interests.

Ethics statement
Human subjects were not included in this study. No animal subjects were included in this study.

Additional information
Supplementary Information The online version contains supplementary material available at https://doi.org/10.1038/s41598-025-04248-1.

Correspondence and requests for materials should be addressed to M.U.K. or H.-H.K.

Reprints and permissions information is available at www.nature.com/reprints.

Publisher's note Springer Nature remains neutral with regard to jurisdictional claims in published maps and institutional affiliations.